ACS NANO
Cite This: ACS Nano XXXX, XXX, XXX−XXX
www.acsnano.org

ARTICLE

Bilayer Lateral Heterostructures of Transition-Metal Dichalcogenides and Their Optoelectronic Response

Prasana Kumar Sahoo,*[,†,#,▽] Shahriar Memaran,[‡,§,▽] Florence Ann Nugera,[†] Yan Xin,[‡] Tania Díaz Márquez,[†] Zhengguang Lu,[‡,§] Wenkai Zheng,[‡,§] Nikolai D. Zhigadlo,[∥,⊥] Dmitry Smirnov,[‡,§] Luis Balicas,*[,‡,§] and Humberto Rodríguez Gutiérrez*[,†]

[†]Department of Physics, University of South Florida, Tampa, Florida 33620, United States
[‡]National High Magnetic Field Laboratory, Florida State University, Tallahassee, Florida 32310, United States
[§]Department of Physics, Florida State University, Tallahassee, Florida 32306, United States
[∥]Department of Chemistry and Biochemistry, University of Bern, Bern 3012, Switzerland
[⊥]CrystMat Company, Zurich 8046, Switzerland

Supporting Information

ABSTRACT: Two-dimensional lateral heterojunctions based on monolayer transition-metal dichalcogenides (TMDs) have received increasing attention given that their direct band gap makes them very attractive for optoelectronic applications. Although bilayer TMDs present an indirect band gap, their electrical properties are expected to be less susceptible to ambient conditions, with higher mobilities and density of states when compared to monolayers. Bilayers and few-layers single domain devices have already demonstrated higher performance in radio frequency and photosensing applications. Despite these advantages, lateral heterostructures based on bilayer domains have been less explored. Here, we report the controlled synthesis of multi-junction bilayer lateral heterostructures based on MoS_2-WS_2 and $MoSe_2$-WSe_2 monodomains. The heterojunctions are created *via* sequential lateral edge-epitaxy that happens simultaneously in both the first and the second layers. A phenomenological mechanism is proposed to explain the growth mode with self-limited thickness that happens within a certain window of growth conditions. With respect to their as-grown monolayer counterparts, bilayer lateral heterostructures yield nearly 1 order of magnitude higher rectification currents. They also display a clear photovoltaic response, with short circuit currents ~10^3 times larger than those extracted from the as-grown monolayers, in addition to room-temperature electroluminescence. The improved performance of bilayer heterostructures significantly expands the potential of two-dimensional materials for optoelectronics.

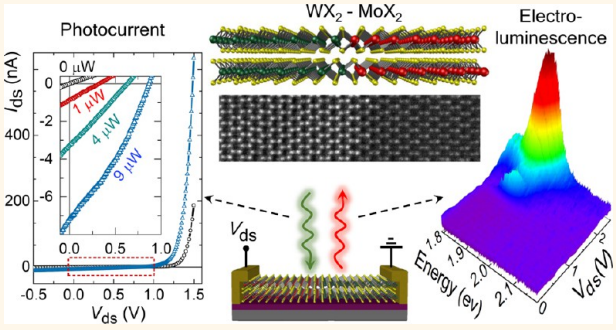

KEYWORDS: *transition-metal dichalcogenides, two-dimensional materials, heterostructures, Raman spectroscopy, photovoltaic, electroluminescence, optoelectronics*

The integration of distinct transition-metal dichalcogenide (TMD) monolayers on the same substrate has seen tremendous progress in recent years *via* the use of chemical vapor deposition techniques.[1−11] It is possible to grow wafer size high-quality films[1,2] of these compounds or even vertical[4] and lateral heterostructures composed of monolayers with distinct band gaps.[3−10] Bilayer TMDs are advantageous because of their environmental stability and potential use in optoelectronics that includes photovoltaics,[12,13] transistors, and logic circuits with relatively higher mobilities compared to the monolayer-based devices.[14−16] They also present attractive physical properties associated with their distinctive crystal symmetry; for instance, robust valley polarization and valley coherence[17] as well as the possibility of electrically tuning the valley magnetic moment.[18] A bilayer vertical heterojunction formed by stacking TMDs monolayer with relative crystalline rotation and/or different lattice constants between two layers leads to the observation of moiré excitons,[19−22] topological excitons,[23] and the realization of exciton-based switches at room temperature.[24] Most of

Received: June 24, 2019
Accepted: September 18, 2019
Published: September 18, 2019

DOI: 10.1021/acsnano.9b04957
ACS Nano XXXX, XXX, XXX−XXX

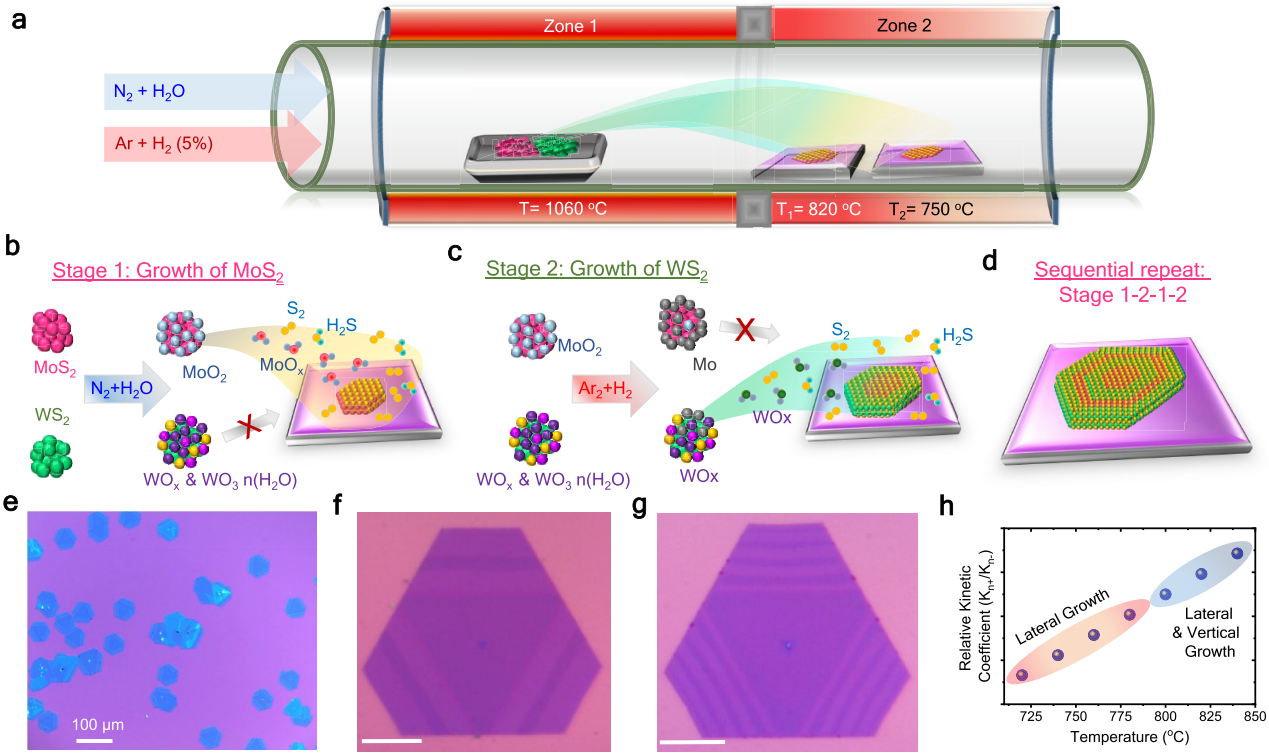

Figure 1. Bilayer lateral heterostructures growth. (a) Schematic of the CVD setup for the synthesis of MoS_2-WS_2 lateral heterostructures. Schematic representation depicting the growth mechanism involved in the growth of (a) MoS_2 domain, (b) WS_2 domain, and (d) showing the sequential repetition of stages 1 (b) and 2 (c) for the growth of multi-junction lateral heterostructures. (e) Optical image of the bilayer MoS_2-WS_2 lateral heterostructures and (f) the corresponding magnified image and (g) multi-junction showing the presence of well-defined domains of MoS_2 and WS_2. Scale bar in (f, g) is 10 μm. (h) K_{n+}/K_{n-} as a function of temperature, as temperature increases, the growth changes from lateral growth to a combination of lateral and vertical growth.

these studies were demonstrated *via* mechanical exfoliation of individual TMD flakes. This method is still posing an issue related to interfacial contamination during the transfer process.

For monolayer devices, there is a large variety of reported performances for a given TMD material, and this variability among reports could have its origin at different material qualities as well as the high sensitivity of the monolayers with respect to the environmental conditions. Substrate roughness and impurities as well as gas adsorbates can introduce unwanted scattering mechanisms for the charge carriers that are detrimental to device performance. Monolayers are also very sensitive to humidity and aging (see Figure S1). Encapsulation could minimize this problem improving device performance.[25,26] Another alternative is to fabricate devices based on few-layers crystals that, in some applications, have shown superior performance when compared to their monolayer counterparts.[27−30] In this sense, lateral heterostructures based on bilayers of TMDs materials are expected to be a more robust system, both in terms of chemical stability and a lower susceptibility to substrate quality or environmental conditions, while maintaining the potential for low-power and flexible optoelectronics offered by monolayers. Thicker lateral heterostructures also provide a longer photon vertical path through the junction, which increases photon absorption[31] (Figure S2) and hence the probability of electron−hole pairs generation.

Despite the potential advantages mentioned above, studies on lateral heterostructures based on bilayer or few-layers TMDs are scarce, mostly because they represent a greater challenge from the synthesis point of view. More recently, we reported a rather simple and scalable chemical vapor deposition (CVD) method to create an undefined number of lateral heterojunctions with epitaxially grown monolayer domains of distinct binary TMD compounds and their ternary alloys.[9] In the present work we use this method to demonstrate the synthesis of multi-junction lateral heterostructures of bilayer TMD domains. Optical microscopy, micro-Raman and photoluminescence (PL) spectroscopy, as well as atomic resolution Z-contrast imaging by electron energy loss spectroscopy (EELS) in an aberration-corrected scanning transmission electron microscope (STEM) with a high-angle annular dark-field detector (HAADF) were used to evaluate the structural and optical quality of the bilayer heterostructures. Using a field effect transistor (FET) geometry, we further evaluated their optoelectronic characteristics including photovoltaic response and room-temperature electroluminescence (EL).

RESULTS AND DISCUSSION

Direct Growth of Bilayer MoX_2-WX_2 (X = S, Se) Lateral Heterostructures. The bilayer lateral heterostructures were synthesized directly on SiO_2/Si substrates following our previously reported one-pot water-assisted CVD approach.[9] This synthesis approach is depicted in Figure 1a. The substrates were placed downstream at temperatures between 725 and 810 °C, while MoX_2 and WX_2 powder sources are placed in an alumina boat at 1060 °C upstream. The direct growth of multi-junction MoX_2-WX_2 lateral heterostructures can be summarized as follows. Stage 1: N_2 gas, bubbled through H_2O, interacts with the MoX_2 and WX_2 powder

DOI: 10.1021/acsnano.9b04957
ACS Nano XXXX, XXX, XXX−XXX

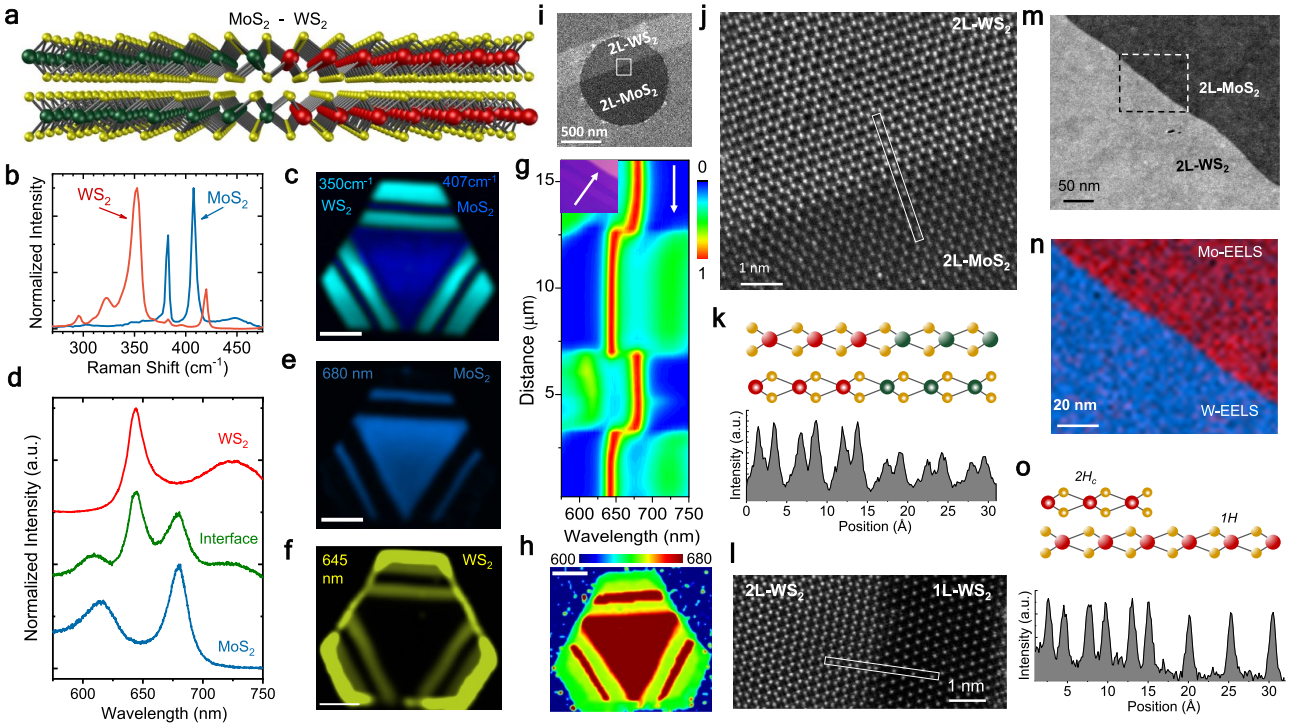

Figure 2. Bilayer MoS_2-WS_2 lateral multi-junction heterostructure and their interfaces. (a) Atomic structure of the bilayer heterostructure from a cross-section perspective, with 2H stacking. (b) Typical Raman spectra of bilayer WS_2 and MoS_2 domains. (c) Composite Raman intensity map including the modes at 405 cm^{-1} (A_{1g}, MoS_2) and 350 cm^{-1} (2LA(M), WS_2) for the heterostructure in Figure 1f. (d) Typical PL spectra of a 2L-WS_2 domain, a MoS_2 domain, and the interface WS_2-MoS_2. PL intensity maps of (e) MoS_2 domains (peak at 680 nm) and (f) WS_2 domain (645 nm) for the structure in Figure 1f. (g) PL line scan and (h) PL position map for the peak maxima, corresponding to the structure in Figure 1f. (g) Contour color plots of the normalized PL intensity as a function of the position across the three-junctions (inset optical image), where the white arrows indicate the direction of the line map. Scale bars correspond to 10 μm. (i) HAADF-STEM image of a lateral heterostructure section. (j) Atomic-resolution STEM image of an atomically sharp bilayer lateral heterojunction. (k) Scattered electron intensity profile (along the line in (j)) and its corresponding ball model from a cross-sectional perspective. (m) Lower magnification Z-contrast images from a bilayer lateral heterojunction and (n) its corresponding EELS maps of the Mo-L and W-L edges. (l) Atomic-resolution STEM image of a thickness transition from bilayer $2H_c$ WS_2 to monolayer 1H WS_2. (o) Scattered electron intensity profile (along the line in (l)) and its corresponding ball model of the cross-section perspective.

sources at 1060 °C forming the gaseous byproducts that are transported downstream to the substrate kept at a lower temperature (Figure 1b). These gaseous species include metal oxides, hydroxides, and chalcogen-containing vapors (*e.g.*, S_2, Se_2, H_2S, H_2Se, *etc.*).[9] Once the gaseous species reach the lower temperature zone (between 800 and 600 °C), they experience a reverse reaction, reducing the metal oxides and incorporating the chalcogen atoms to form the TMDs crystallographic domains at the substrate surface. In the methods section of ref 9 the most important chemical reactions are described in detail. MoO_2 species interact with the chalcogen precursors forming MoX_2 nucleation sites that lead to the growth of MoX_2 domains. Meanwhile, WX_2 precursor undergoes a series of oxidation processes forming higher suboxide phases (WO_x, x = 2−3) and hydroxides. Due to the high volatility of tungsten-based hydroxides, it does not contribute to the growth when in the presence of high H_2O vapor content (Figure 1b). Stage 2: The carrier gas is switched from N_2 + H_2O to Ar + H_2 (5%). This terminates the growth of the MoX_2 domain and favors the growth of WX_2 at the exposed crystal edges. The role of H_2 is to suddenly deplete the MoO_2 to metallic Mo on the surface of the MoX_2 powder source and hence stops the supply of the MoO_2 precursor (Figure 1c). In contrast, the tungsten hydroxides are depleted and the W suboxide (WOx) formed during the previous stage, while at its surface, the powder source continues to evaporate (Figure 1c). Multi-junction lateral bilayer heterostructures of MoX_2-WX_2 can thus be realized by sequentially changing only the carrier gas from N_2 + H_2O to Ar + H_2 (Figure 1d).

The lateral dimensions of individual TMD domains were independently controlled only by varying the respective carrier gases flow times. Although higher temperatures usually favor the growth of few-layer structures, we observe that lateral heterostructures (Figure 1e−g) composed of either monolayers, bilayer, or multi-layers can also grow at a similar range of substrate temperatures (Figure S3a−d), while their relative concentration can be tuned by changing the adatom flux, that is, increasing the precursor concentration in the carrier gas (Figures S4 and S5). In our synthesis method, the concentration of gas precursors can be achieved in different ways, that is, changing the amount of material in the powder source, controlling the temperature of the water in the bubbler, and/or changing the carrier gas flow. Since so many parameters can control the flux of gas precursors, the set of optimal parameter for lateral growth with self-limited thickness (1L, 2L, or multi-layers) is not unique.

Bilayer MoS_2-WS_2-Based Lateral Heterostructures. Figure 1e shows the large-scale image of uniformly distributed bilayer MoS_2-WS_2 lateral heterostructures. Magnified images in Figure 1f,g clearly show the existence of three- and seven-

DOI: 10.1021/acsnano.9b04957
ACS Nano XXXX, XXX, XXX−XXX

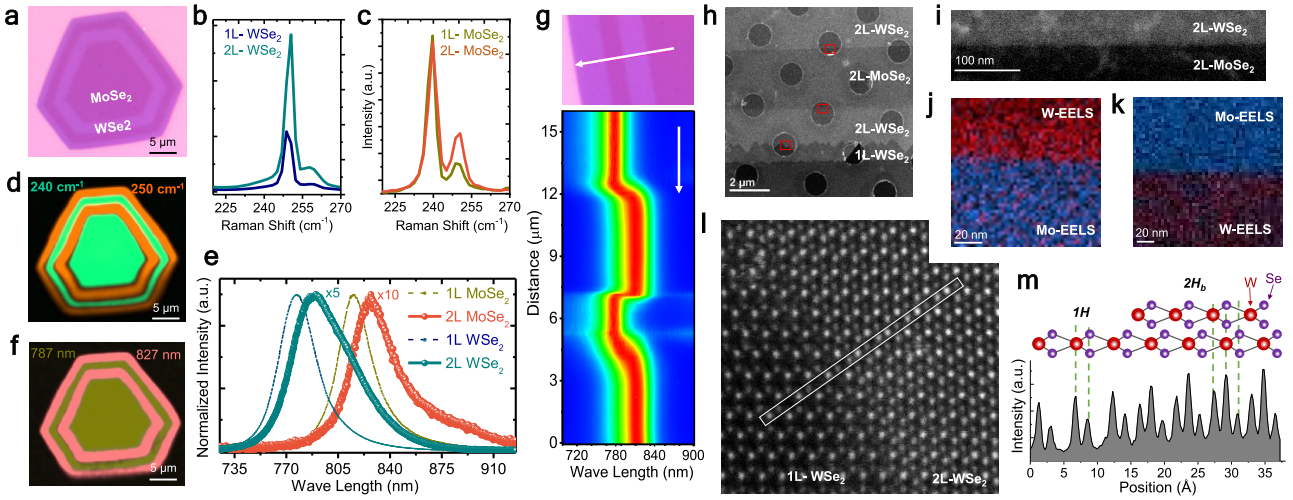

Figure 3. Bilayer $MoSe_2$-WSe_2 lateral multi-junction heterostructures and interfaces. (a) Optical image of a three-junction bilayer $MoSe_2$-WSe_2 lateral heterostructure. (b) Raman spectra of 1L- and 2L-WSe_2 domains. (c) Raman spectra of 1L- and 2L-$MoSe_2$ domains. (d) Composite Raman intensity map at the frequency 250 cm^{-1} (A_{1g} mode of 2L-WSe_2) and at 240 cm^{-1} (A_{1g} mode of 2L-$MoSe_2$). (e) Normalized PL spectra of 1L- and 2L-WSe_2 as well as 1L- and 2L-$MoSe_2$ domains. (f) Composite PL intensity map using the 788 nm (2L-WSe_2) and 827 nm (2L-$MoSe_2$) peaks. (g) Top panel: Optical image (section) of a bilayer $MoSe_2$-WSe_2 lateral heterostructure. Lower panel: Normalized PL color contour plot across the white line in the top panel. (h) Low-magnification HAADF-STEM image of a bilayer (2L) WSe_2-$MoSe_2$-WSe_2 lateral heterostructure. (i) Higher magnification Z-contrast image of the junction at the top red square in (h). (j, k) Elemental EELS maps for the top and middle bilayer lateral junctions (red squares in (h)), respectively. (l) Atomic resolution STEM image of the 2L-1L transition region (bottom red square in (h)). (m) Scattered electron intensity profile (along the line in (l)) and its corresponding cross-section depicted through a ball model.

junctions, respectively. The sulfides-based heterostructures predominantly grew as truncated triangles. Figure 2a shows the schematic representation of a typical $2H_c$-type bilayer lateral heterostructure. The representative Raman spectra from WS_2 and MoS_2 individual domains are shown in Figure 2b. The Raman peaks at 354 cm^{-1} (E_{2g} mode), 420 cm^{-1} (A_{1g} mode), and 350 cm^{-1} (2LA(M)) are characteristic of WS_2,[32,33] while the peaks at 383 cm^{-1} (E_{2g}), 407 cm^{-1} (A_{1g}), and 450 cm^{-1} (2LA) correspond to MoS_2 (Figure 2b).[34,35] Notice that the first order peaks (E_{2g} and A_{1g}) present a full-width-at-half-maximum FHWM $\leq$ 5 cm^{-1}, which is typical for high-quality samples.[36,37] Additionally, it has been reported that the 2LA Raman peak shifts to higher wavenumbers as the crystalline disorder increases in MoS_2 films,[37] hence the observation of 2LA at 450 cm^{-1}, in our samples, is another indication of high crystalline quality. The composite Raman intensity map in Figure 2c clearly shows the spatial distribution of laterally connected domains of MoS_2 (407 cm^{-1}) and WS_2 (350 cm^{-1}) bilayers (see additional maps in Supporting Information Figure S6).

The PL spectrum from 2L-WS_2 bilayer domains (Figure 2d) consists of one major peak located at ≅645 nm accompanying a minor broad peak at ≅720 nm. The peak at 645 nm corresponds to a direct excitonic emission at the K and K′ points of the Brillouin zone. In contrast, the peak at 720 nm arises from an indirect electronic transition.[38] Even though the electronic bands in WS_2 evolve from direct to indirect band gap as the number of layers increases,[38,39] bilayer WS_2 still displays a relatively strong direct band gap emission that dominates its PL spectrum. For the 2L-MoS_2 bilayer domains, the typical PL spectrum presents two major peaks around 680 and 606 nm, corresponding to the A and B excitonic transitions, respectively (Figure 2d).[38,40,41] The PL spectrum at the WS_2 → MoS_2 heterointerface (Figure 2d) consists of a superposition of PL peaks from both MoS_2 and WS_2 domains that are simultaneously excited by the laser probe. The absence of alloy-related peaks at intermediate energies suggests the presence of a chemically sharp WS_2 → MoS_2 interface. The PL intensity map (Figure 2e,f) as well as the peak position map (in Figure 2h) are in agreement with the Raman map in Figure 1c, (additional maps in Supporting Information Figure S6). The normalized PL contour plot of a line-scan across three junctions (Figure 2g) provides a better visualization of the abrupt modulation of the band gap. Notice that the transition of the PL signal for WS_2 → MoS_2 interfaces is sharper when compared to MoS_2 → WS_2 interfaces, indicating that the latter might present a small degree of alloying at the junction. The existence of heterojunctions with different composition profiles (sharp or smooth) is intrinsically related to the distinct kinetics of the chemical reactions of Mo- and W-based compounds during the gas switching time. We previously observed a similar trend in monolayer lateral heterostructures.[9]

The atomic structure and the local chemical distribution near the bilayer lateral heterojunctions were studied by atomic resolution Z-contrast imaging and by EELS in an aberration-corrected STEM. Figure 2i shows a low-magnification, HAADF STEM image of a heterostructure section, the 2L-WS_2 domain appears in bright contrast, while the 2L-MoS_2 domain is darker. An atomically sharp bilayer lateral heterojunction is shown in Figure 2j, where the atoms appear brighter in the WS_2 domain due to the higher Z-number. The crystal structure in both domains (2L-WS_2 and 2L-MoS_2) display a hexagonal arrangement (Figure 2j) that is consistent with the $2H_c$ polytype,[42] space-group $P6_3/mmc$. In the $2H_c$ polytype, each transition metal atom, in one layer, is vertically aligned with two chalcogen atoms located in the neighboring layer, and *vice versa* (see schematic in Figure 2k and its corresponding intensity profile). Lower magnification Z-contrast images from a bilayer lateral heterojunction (Figure 2m) as well as elemental EELS maps of the Mo-L and W-L

DOI: 10.1021/acsnano.9b04957
ACS Nano XXXX, XXX, XXX−XXX

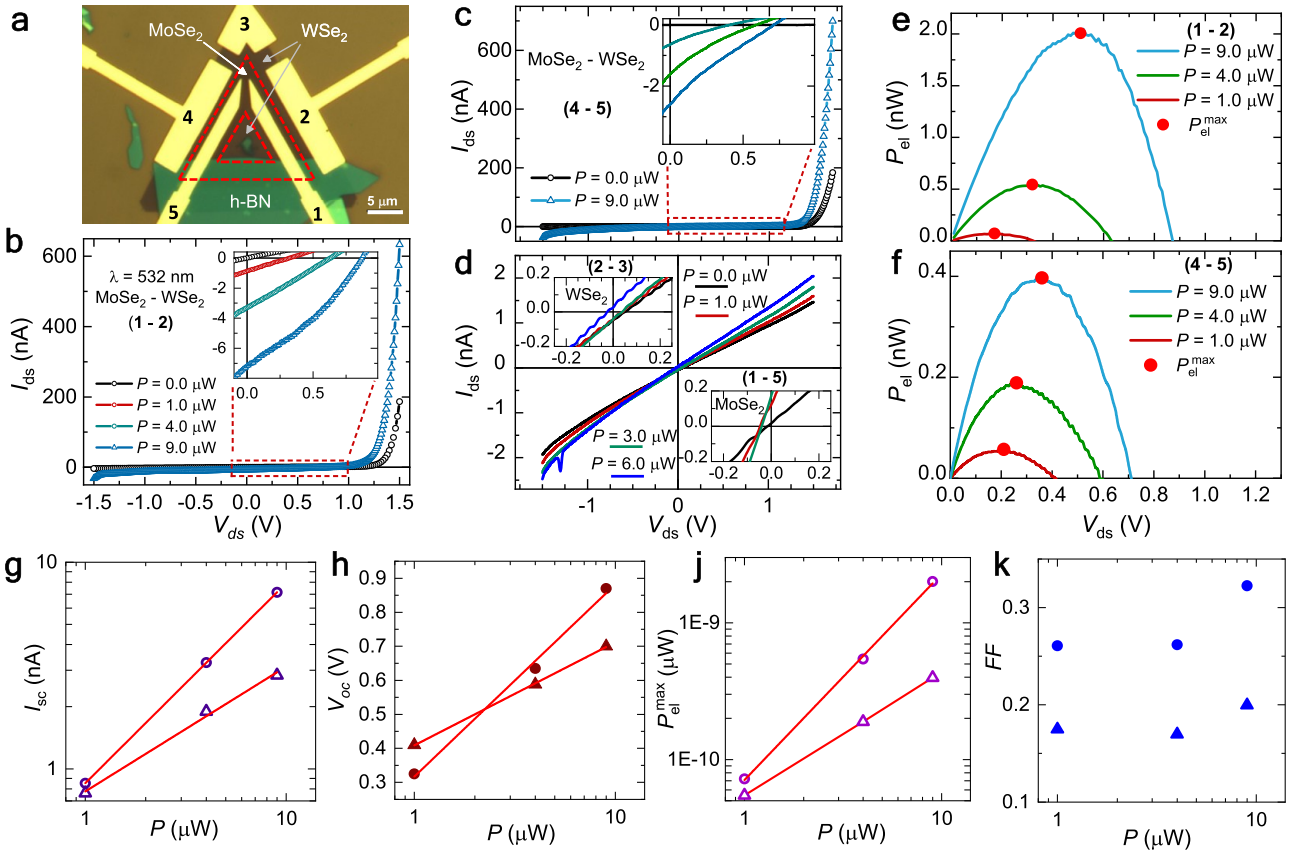

Figure 4. Photovoltaic response across bilayer WSe_2-$MoSe_2$ junctions. (a) Optical image of a bilayer $MoSe_2$/WSe_2 bijunction, red triangles indicate the position of the junctions, gold electrical contacts are in yellow, and h-BN[49] used as an insulating bridge to reach the inner domains appears in green. The response of the $MoSe_2$ domain was characterized *via* two-terminal measurements using the contacts 1−5, while the outer WSe_2 domain through contacts 3−4 and 2−3. The transport across the junctions, particularly under laser illumination (λ = 532 nm), was probed through contacts 4−5 and 1−2. Notice that these pairs of contacts have distinct separations. (b,c) Drain to source current I_{ds} as a function of the bias voltage V_{ds}, for I_{ds} flowing through contacts 1−2 and 5−4, respectively. Both show diode-like responses (or p−n junction behavior) that are considerably enhanced by illumination. The insets are amplified scale plots showing short-circuit currents I_{sc} (for V_{ds} = 0) resulting from the photovoltaic effect. (d) I_{ds} as a function of V_{ds} within individual domains measured through contacts 3−4 (WSe_2, main panel and top inset) and through contacts 1−5 ($MoSe_2$, bottom inset). Notice the absence of a diode-like response and the very small I_{sc} values, that is, in the order of just 0.1 nA. (e,f) Photogenerated electrical power $P_{el} = I_{ds} \times V_{ds}$, under several illumination powers P, measured between leads 1−2 and 4−5, respectively. Red dots indicate the corresponding maxima of P_{el} (P_{el}^{max}), which scale with the illuminated area despite the sharpness of the junctions. (g) Short-circuit current I_{sc}, (h) open-circuit voltage V_{oc}, (j) P_{el}^{max} (violet hollow symbols), and (k) fill factors $FF = P_{el}^{max}/(I_{sc} \times V_{oc})$ (blue filled symbols) as functions of the laser illumination power (P), where circles (triangles) are the values extracted for the junction between leads 1−2 (4−5). Red lines are linear fits, indicating that I_{sc} displays a power law dependence $I_{sc} \propto P^{0.6}$; V_{oc} follows the characteristic semi-logarithmic dependence on P expected for a diode; for $P_{el}^{max} \propto P^{\alpha}$, with α = 1.5 (junction 1−2) and α = 0.9 (junction 4−5).

edges (Figure 2n) also indicate a clear difference in the chemical composition of each domain, which is consistent with the PL and Raman maps discussed above. Figure 2l shows a thickness transition at the outermost edge of the heterostructure from bilayer $2H_c$ WS_2 to monolayer 1H WS_2, consistent with the strong PL from the edge region in Figure 2f. The corresponding scattered electron intensity profile along the $[11\bar{2}0]$ direction is shown in Figure 2o. The distinct symmetry of the atomic contrast between the bilayers and the monolayers, as observed in the STEM images, facilitates their identification. The monolayer at the outermost edge forms at the end of the growth process during the cooling down phase when both the temperature and precursors supply are decreasing. The formation of 2L−1L junctions offers another opportunity for two-dimensional (2D) electronic devices due to the change in band gap as well as band offsets at the interface, as recently demonstrated by Howell *et al.*[43]

Bilayer $MoSe_2$-WSe_2-Based Lateral Heterostructures. Similar to the sulfides, bilayer lateral heterostructures of selenium-based TMDs (2L-$MoSe_2$−2L-WSe_2) were also synthesized using the water-assisted CVD method.[9] Figure 3a displays a three-junction heterostructure with faceted hexagonal geometry, and the 2L-$MoSe_2$ domains appear in a reddish brown color, while 2L-WSe_2 domains are pink (additional optical images in Figures S7). Representative Raman spectra for bilayer (2L) and monolayer WSe_2 and $MoSe_2$ domains are shown in Figure 3b,c, respectively. For the bilayer WSe_2 the A_{1g} phonon mode (at 250.5 cm^{-1}) is blue-shifted by 1 cm^{-1} when compared to the monolayer, while the peak at 257.5 cm^{-1} (2LA(M)) is red-shifted by 2.5 cm^{-1}. The frequency difference $\Delta\omega$ [2LA(M) − A_{1g}] is 7 cm^{-1} for bilayers and 11 cm^{-1} for monolayers, in agreement with previous reports.[44] In bilayer $MoSe_2$, the characteristic phonon modes (Figure 3c) were observed at 240 cm^{-1} (A_{1g} mode) and at 249.5 cm^{-1} ($E_{2g}^2(M)$ shear mode). In contrast to bilayer

DOI: 10.1021/acsnano.9b04957
ACS Nano XXXX, XXX, XXX−XXX

WSe_2, the difference in frequency $\Delta\omega$ $[E^2_{2g}(M) - A_{1g}]$ for bilayer $MoSe_2$ is negligible. However, the intensity ratio $A_{1g}/E^2_{2g}(M)$ decreases by 76% in bilayer $MoSe_2$ when compared to its monolayer. Figure 3d displays the composite Raman intensity map at frequencies of 250 cm^{-1} (2L-WSe_2) and 240 cm^{-1} (2L-$MoSe_2$), and the color pattern agrees with the optical contrast in Figure 3a.

We observed a clear dependence of the PL spectra with the number of layers in both WSe_2 and $MoSe_2$ domains as shown in Figure 3e (see also Figure S3), in agreement with previous reports.[38,44,45] In bilayer WSe_2, the PL peak corresponding to the direct excitonic emission appears at 788 nm, which is shifted by $\Delta E = E_{1L} - E_{2L} = 8.6$ meV when compared to the monolayer. The shoulder at ~811 nm is associated with the indirect bandgap optical transition. Similarly, for bilayer $MoSe_2$, the direct and indirect band transitions are located at 827 and 893 nm, respectively,[45] with a direct bandgap shift of $\Delta E = E_{1L} - E_{2L} = 9$ meV with respect to the monolayer. The PL signal from the bilayer domains (WSe_2 and $MoSe_2$) is rather broad and exhibits relatively strong emissions, typical of high-quality materials. Composite PL intensity maps (Figure 3f) at 788 nm (2L-WSe_2) and 827 nm (2L-$MoSe_2$) further confirm the homogeneity of the PL signal within each domain (Figure S7). A PL line-scan perpendicular to the three-junctions (Figure 3g) also confirms the sequential modulation of the bandgap across the heterostructure. Note that, similar to our observations in Figure 2g for the sulfides-based heterostructures, the change in the position of the PL peak at the $WSe_2 \rightarrow MoSe_2$ junction is sharp when compared to the $MoSe_2 \rightarrow WSe_2$ interfaces (Figure 3g). For the latter, the smooth change in the PL peak position across the interface suggests the presence of a compositional gradient, which contrasts with the sharp chemical transition observed for the $WSe_2 \rightarrow MoSe_2$ junctions. This trend does not depend on the type of chalcogen atom, but, as mentioned before, on the different oxidation−reduction kinetics of the Mo and W precursors.[9]

A low-magnification HAADF-STEM image of a bilayer (2L) WSe_2-$MoSe_2$-WSe_2 lateral heterostructure is shown in Figure 3h. The 2L-WSe_2 domain appears in bright electronic contrast, while the 2L-$MoSe_2$ domain is darker. The spatial chemical distribution observed from Z-contrast images (Figure 3i) as well as elemental EELS maps (Figure 3j,k) also confirms the formation of laterally connected 2L-WSe_2 and 2L-$MoSe_2$ domains, in agreement with the Raman and PL data shown in Figure 3d,f. Atomic resolution STEM images of the different interfaces are shown in the supplementary data (Figure S8). Similar to the case of the sulfides, there is a 1L-WSe_2 fringe domain at the outermost border of the heterostructure, probably formed due to a reduction in precursors supply at the end of the synthesis process during the sample cooling (Figure 3h). Atomic resolution imaging of this 2L-1L transition region (Figure 3l) shows the distinct crystal symmetries of the 2L-WSe_2 and the 1L-WSe_2 domains. In contrast with the $2H_c$ stacking observed in the sulfide bilayers, the symmetry observed for the selenide bilayers is more consistent with a $2H_b$ stacking,[42] space group $P\bar{6}m2$, as depicted by the ball model in Figure 3m.

The $2H_b$ stacking is the bilayer equivalent of the 3R stacking, and the $2H_c$ is commonly known as 2H stacking only; both phases have been observed in sulfides and selenides. Although the conditions favorable for either phase are not well understood, a recent publication[46] reported the simultaneous synthesis of bilayer islands of WS_2 and WSe_2 with certain degree of control over the stacking type. In that work, the $2H_c$ stacking was formed at slightly higher temperatures than the $2H_b$ stacking. They also observed that $2H_c$ islands were mainly hexagonal, while the island with $2H_b$ stacking were triangular. Additionally, it has been well established that the edge stability, and consequently the formation of hexagonal or triangular islands, depends on the concentration ratio of metal to chalcogen atoms in the vapor precursors.[47,48] This suggests that the formation of either $2H_c$ or $2H_b$ phases might obey to a nontrivial interplay between growth temperature and metal-to-chalcogen ratio of the precursors. In our experiments, we have observed that sulfides exhibit predominantly truncate triangular geometry, while the selenides display both hexagonal and triangular geometries. According to our observations, and consistent with the report by Zeng *et al.*,[46] we expect that both phases ($2H_c$ and $2H_b$) can form depending on the local metal-to-chalcogen concentration ratio in the vapor precursors.

Electrical Performance of Bilayer $MoSe_2$-WSe_2 Lateral Heterostructures. In order to evaluate the optoelectronic properties of the bilayer lateral heterostructures, a particular configuration of metallic contacts has been designed to probe the electrical transport of the individual domains as well as the transport properties across their junctions (Figure 4a). The bilayer heterostructure in Figure 4a is composed of three concentric triangular domains ($MoSe_2$-WSe_2-$MoSe_2$), and their junctions are highlighted by the red dashed lines. $I-V$ characteristics measured across the junctions (*i.e.*, across contacts 1−2 or 4−5, black symbols in Figure 4b,c, respectively), show a clear diode-like response. The dark currents $I_{ds} \approx 200$ nA measured in forward bias ($V_{ds} > 0$) and $I_{ds} \approx 3.5$ nA measured in reverse bias (-1.5 V $< V_{ds} < 0$), result in a 10^2 ratio between forward and reverse biases. Under illumination conditions, the I_{ds} in direct bias increases by a factor of 3. Similarly to the monolayers,[9] this marked nonlinearity cannot be attributed to Schottky barriers at the level of contacts given the nearly linear $I-V$ characteristics of individual domains, or the clear lack of a diode-like response as well as a pronounced increase in the photoresponse upon illumination, see Figure 4d (expanded scale in Figure S9a).

The doping type for each individual domain, p-type WSe_2 and n-type $MoSe_2$, was determined by measuring the drain-source current (I_{ds}) as a function of back-gate voltage V_{bg} (Figure S9c). For these measurements, the heterostructures were transferred onto fresh SiO_2 layers since the original ones were affected by the presence of pinholes resulting from the synthesis protocol. This transfer process is detrimental to the quality and therefore to the performance of the individual domains. Hence, in Figure S9 the slopes of I_{ds} as a function of V_{bg} are not a good measure of the intrinsic mobilities of these domains.

The $I-V$ characteristics across the junctions, shown in magnified scales in the insets of Figure 4b,c, reveal the existence of a finite current under zero bias which scales with the illumination power, this photovoltaic-effect was not previously observed by us in the corresponding monolayer heterostructures.[9] Notice that excepting the observation of this short-circuit current, the overall photodiode-like response of these bilayers, that is, the photocurrent extracted under a given illumination power, is comparable to those obtained by us from monolayers.[9] It is important to mention that the nonzero currents observed at zero voltages in both insets in Figure 4d are an experimental artifact associated with poor grounding.

DOI: 10.1021/acsnano.9b04957
ACS Nano XXXX, XXX, XXX−XXX

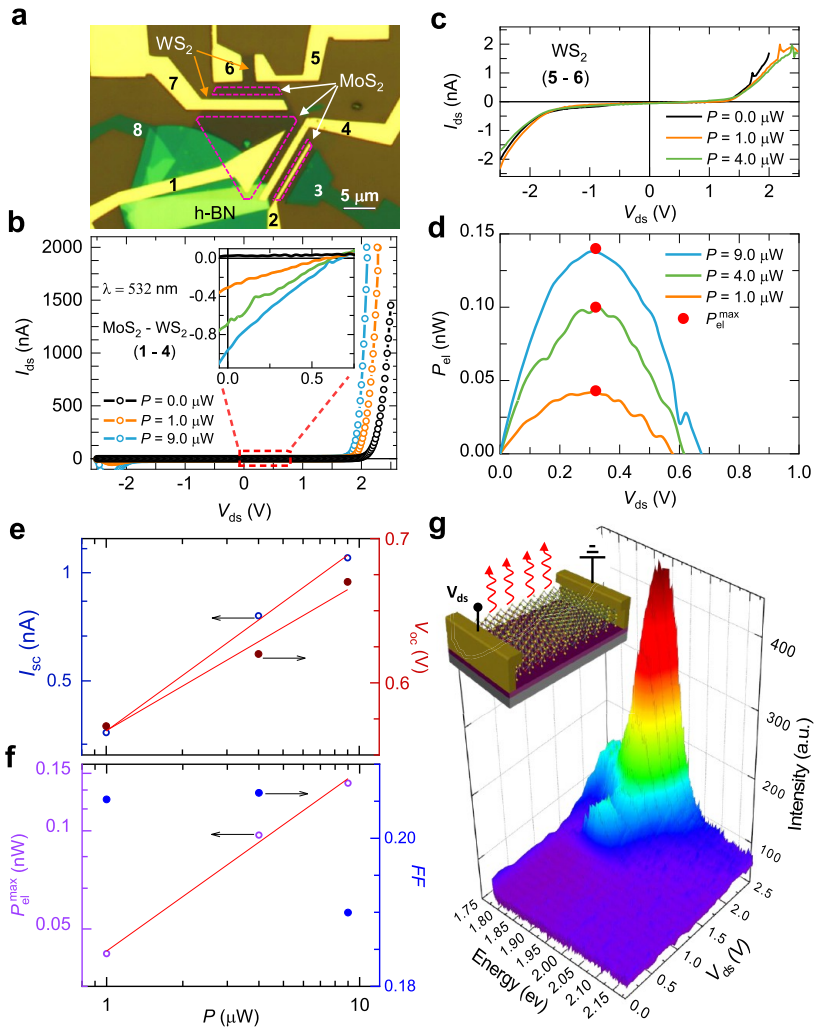

Figure 5. Optoelectronic response of bilayer MoS_2-WS_2 junctions. (a) Optical image of a bilayer MoS_2/WS_2 three-junctions heterostructure, the junctions are highlighted by the magenta dashed lines, and gold pads electrical contacts are in yellow. The optoelectronic response of the outer WS_2 domain was characterized through contacts 5−6, while the transport across the junction was probed through contacts 1−4. (b) I_{ds} as a function of V_{ds} measured across the junction (1−4), for different laser illumination powers (λ = 532 nm). Inset: Magnified scale within the dashed rectangle (around V_{ds} = 0) showing a significant short-circuit current I_{sc} resulting from the photovoltaic effect. (c) I_{ds} *vs* V_{ds} for currents flowing between contacts 5−6 (WS_2 domain), showing a nonlinear *I*−*V* characteristic due to the Schottky barriers at the electrical contacts. Upon illumination the diode current across the junction is 10^3 times higher than the nonlinear current flowing across a single domain. (d) Photogenerated electrical power P_{el} under different illumination powers *P* for currents flowing between leads 1−4. Red dots indicate the corresponding P_{el}^{max}. (e) Short-circuit current I_{sc} (blue hollow symbols) and open-circuit voltage V_{oc} (brown filled symbols) extracted for the junction (1−4). The red linear fit for I_{sc} is a power law $I_{sc} \propto P^{0.5}$. The red linear fit for V_{oc} follows the characteristic semi-logarithmic dependence on *P*. (f) P_{el}^{max} (violet hollow symbols) and *FF* (blue filled symbols) as functions of *P*. The red line is a linear fit yielding $P_{el}^{max} \propto P^{0.6}$. (g) Room-temperature EL response from a bilayer MoS_2-WS_2 lateral heterostructure.

Notice that these rather small currents do not scale with the illumination power, indicating that they do not result from the Schottky diodes at the contacts.

One could expect a marked difference in behavior between monolayers and bilayers given the difference in their gap sizes. However, there are extrinsic factors playing probably a more relevant role for their photoresponse such as the interaction with the substrates and adsorbates. Bilayers should be less sensitive to both effects. In addition, their smaller band gaps could lead to a smaller band misalignment with respect to the metallic contacts. This confluence of facts would explain their enhanced photoresponse with respect to that of the monolayers. Returning to the photovoltaic response, one should bear in mind that conventional solar cells are typically vertical p−n junctions and that the photovoltaic power conversion efficiency (η) is calculated as the ratio between the maximum photogenerated electrical power $P_{el}^{max} = I_{ds} \times V_{ds}$ and the illumination power. Vertical p−n junctions cover the entire illuminated area, regardless of the sharpness of the junction along the vertical direction. Notice that for lateral junctions, the area of the junction is considerably small when compared to the total illuminated area. As shown in Figure 2j, the lateral junctions can be atomically sharp extending by a distance of <1 nm at the interface between both domains and are only two monolayers thick (1.2 nm). Thus, taking in to account the laser spot size of 10 μm (diameter), regardless of whether we consider the cross-sectional area or the in-plane area of the junction, the calculated area will be $A_j \cong 10^{-2}$ μm^2. Therefore, a laser illumination power of 1 μW would provide only 1.27×10^{-4} μW to the junction area, and the calculated

DOI: 10.1021/acsnano.9b04957
ACS Nano XXXX, XXX, XXX−XXX

efficiencies would be extremely high. To address this point, we fabricated contacts that expose distinct areas of the material surrounding the junctions, observing that the short circuit current or $I_{sc} = I_{ds}$ (when $V_{ds} = 0$ V) seems to scale with the illuminated area. In effect, we estimate illuminated areas of ~21.6 μm^2 and 10.8 μm^2 between contacts 1−2 and 4−5, respectively, with corresponding I_{sc} values of ≅ 3 nA and 9 nA under 9 μW of laser illumination power (λ = 532 nm). Therefore, these areas receive effective illumination powers P = 2.48 μW and 1.23 μW, respectively, which can be contrasted to the extracted maxima photovoltaic electrical power P_{el}^{max} = 2 nW and 0.4 nW, as indicated by the red dots in Figure 4e,f, respectively. These numbers would lead to modest power conversion efficiencies $\eta = 100 \times P_{el}^{max}/P \cong 0.08\%$ and 0.03%, respectively. Notice that if we use the previously estimated value of A_j to calculate η, one would obtain values that are ~10^3 higher. If instead, we used the estimation of the depletion width provided in ref 7 for lateral junctions or widths ranging between 92 and 515 nm (depending on the doping level), one would obtain power conversion efficiencies ranging between 0.13 and 1.9%. These values are considerably higher than η = 0.2% reported in ref 7, although our fill factors are similar, see text below. Therefore, future work should focus in defining, unambiguously, the effective width of the junctions in lateral heterostructures as the ones studied here. However, small η can be attributed to a number of factors, like the detrimental role played by the Schottky barriers, or the relatively small probability of generating electron−hole pairs by photons traveling through quite thin layers (low optical absorption). Nevertheless, one can envision a number of strategies to improve the conversion efficiency, that is, use of reflective back layers, metals with distinct work functions for the electrical contacts, or the addition of extra layers to increase the efficiency of these heterostructures.[50] Figure 4g,h displays I_{sc}, the open-circuit voltage V_{oc}, P_{el}^{max}, and the photovoltaic fill factor $FF = P_{el}^{max}/(I_{sc} \times V_{oc})$ as functions of the illumination power P. I_{sc} and P_{el}^{max} are observed to display a power law dependence on P as previously observed in multi-layered junctions.[51] V_{oc} displays the typical semi-logarithmic dependence on P: $V_{oc} = nkT/q \ln(I_L/I_0 + 1)$, where n is the carrier density, q is the charge of the carrier, and I_L is the photogenerated current. Since I_L scales with the illumination power, one expects V_{oc} to display a logarithmic dependence on P. FF shows very modest values, that is, between 0.2 and 0.3, which are considerably smaller than the values extracted from conventional solar cells,[50] indicating that there is ample room for improvement in performance.

Optoelectronic Performance of Bilayer MoS_2-WS_2 Lateral Heterostructures. The contacts configuration employed to study the electrical properties of lateral heterojunctions composed of MoS_2 and WS_2 bilayer domains is shown in Figure 5a. Similar to the selenides, the individual domains display a p-type behavior for the WS_2 and n-type for MoS_2 (Figure S9b). A clear diode-like response is observed for the $I-V$ characteristic measured between contacts 1−4, that is, from the central MoS_2 bilayer domain toward the WS_2 outer domain (Figure 5b). There is a pronounced photoinduced increase in the forward bias current. The MoS_2-WS_2 bilayers lateral junctions also display a clear photovoltaic response which is comparable in magnitude to that observed for $MoSe_2$-WSe_2 heterojunctions, and the corresponding short-circuit currents are shown in the inset of Figure 5b. The $I-V$ characteristic corresponding to the WS_2 single domain (Figure 5c), measured through contacts 5−6, is nonlinear, indicating a more prominent role for the Schottky barriers around the contacts when compared to the Se-based heterostructures. However, it does not display a clear diode-like response, the currents are 3 orders of magnitude inferior with respect to the forward biased currents observed across the junction, and the effect of illumination is barely observable. This clearly indicates that the Schottky barriers play little to no role in the diode-like response observed in MoS_2-WS_2 bilayer heterojunctions. Here, it is important to emphasize that we did not detect any photovoltaic response in monolayers, implying again that this response cannot be attributed to Schottky diodes at the contacts, otherwise it would have been observed in both bilayers and monolayers. Although a detailed mapping of the photocurrent[13,43,52] extracted from our samples would be desirable, it is not required to conclude, unambiguously, that the observed photovoltaic response is intrinsic to the junctions.

The photogenerated electrical power is plotted in Figure 5d. The illuminated area between the electrical contacts is 16 μm^2, which represents ~1/5 of the total laser spot area, hence 1 μW in laser power actually corresponds to an incident power P = 0.2 μW. According to Figure 5d, this yields a photogenerated P_{el}^{max} = 0.043 nW and thus an efficiency $\eta = 100 \times P_{el}^{max}/P$ = 0.02% which is comparable to the values previously extracted for the Se-based heterojunctions. In these calculations we have assumed conservatively that the entire area of the exposed channel contributes to the photovoltaic response, but these values would become much larger if one considered depletion widths as calculated in ref 7. Figure 5e,f displays I_{sc}, V_{oc}, P_{el}^{max}, and FF as functions of the incident power P in a logarithmic scale. As previously seen for the Se-based bilayer heterojunctions, both I_{sc} and P_{el}^{max} follow a power law dependence on P, with V_{oc} displaying the canonical semi-logarithmic dependence on P. FF on the other hand displays lower values, that is, below 0.21, indicating a slightly inferior performance, possibly resulting from larger Schottky barriers as implied by the nonlinear $I-V$ characteristics of the individual domains.

Finally, the devices based on bilayer MoS_2-WS_2 lateral heterostructures exhibit EL at room temperature as shown in Figure 5g. The EL signal is observed for bias voltages between 1.5 and 2.5 V. The position of the EL peak maximum is between 1.91 and 1.94 eV, which is similar to the 1.92 eV direct excitonic emission in the PL spectrum of 2L-WS_2 domains (Figure 2g). Interestingly, these EL energy values are also comparable to the average energy (1.94 eV) between the most prominent peaks, excitons A and B, in the PL spectrum of the 2L-MoS_2 domains (Figure 2g). We have observed that the PL signal is considerably stronger in WS_2 than MoS_2, suggesting that the radiative electron−hole recombination process is more efficient in WS_2 and hence that the EL signal could be generated mainly in the 2L-WS_2 side of the junction. However, the EL peak is asymmetric toward lower energies, therefore a small contribution to the EL signal from electron−hole recombination (exciton A) in the 2L-MoS2 domain cannot be ruled out. Finally, notice that 1.94 eV corresponds to photons in the visible spectra, of red color approaching orange, which makes these junctions potential candidates for developing light-emitting devices.

Mechanism for Lateral Growth with Self-Limited Thickness. In van der Waals solids, the thermodynamic[53] and kinetic[53,54] factors responsible for the competition between lateral and vertical epitaxy are still under debate.[14,53−55] In mass-driven kinetic reactions, a linear

DOI: 10.1021/acsnano.9b04957
ACS Nano XXXX, XXX, XXX−XXX

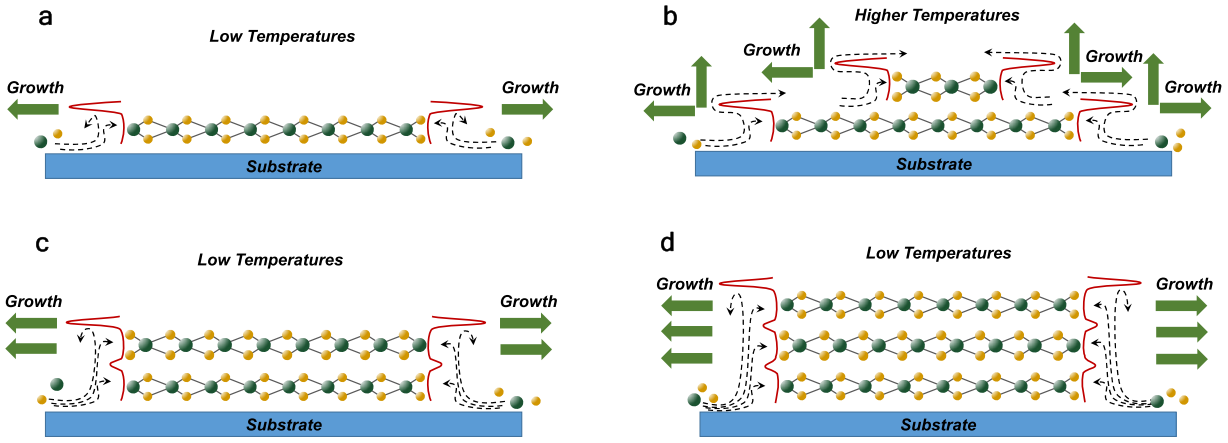

Figure 6. Phenomenological growth model. (a,c,d) Lateral growth at low temperatures with self-limited thickness. (b) At higher temperatures, both lateral and uncontrolled vertical growths are allowed. We proposed a model where in the early stages of the growth, the initial nanoclusters can have one or few layers with adjacent stacked edges. The adjacent edges will reduce the barrier for adatoms hopping between layers, but the barrier at the top layer is still high enough to prevent adatoms from climbing to the top surface of the structure (c,d). At low temperatures, this vertical profile of the potential energy allows the diffusion and subsequent attachment of adatoms in all the edges, while the higher energy barrier at the top will prevent the vertical growth of additional layers, resulting in the simultaneous lateral growth of all the layers, with self-limited thickness (a,c,d).

relation between the amount of adatom flux and the domain size is expected.[14] However, we have not observed any systematic increase in domain size while increasing the amount of precursor, rather we observe the promotion of vertical growth. Further increasing the amount of precursor leads to a decrease in domain size and the formation of uncontrolled multi-layer domains which can be ascribed to the breakdown of self-limiting growth with increasing adatom flux. In CVD growth, it is simplistic to assume that by placing substrates in different positions along the furnace temperature profile, only the temperature of the substrate will be different; there is also a gradient in the concentration of the gas precursors that increases as the distance to the solid source decreases. For instance, in a same growth we have observed that the closer the substrate is to the source, the higher the number of layers in the lateral heterostructure (Figure S5). Temperature plays a key role in the final outcome of the growth, that is, at low temperatures, the lateral growth is promoted, while higher temperatures favor vertical growth; this is also valid for the case of heterostructures.[4] Ye *et al.*[54] proposed a multi-scale model where the ratio of kinetic coefficients accounting for the attachment (K_{n-}) and detachment (K_{n+}) of adatoms to the edge of the growing layer (n) is linked to the temperature through the expression $K_{n+} = K_{n-} \exp(-V_b/kT)$, where V_b is the energy barrier that adatoms most overcome to climb to the top surface of the layer. This barrier is equivalent to the Schwoebel step-edge barrier in non-van der Waals solids.[56] At low temperatures, the adatoms do not have sufficient energy to overcome the edge-energy barrier (red line in Figure 6a) to hop from the substrate to the top surface of the TMD layer. Hence, they form stable chemical bonds at the edge of the film, resulting in lateral growth. At higher growth temperatures, the kinetic coefficient K_{n+} approaches K_{n-}, and the adatoms will have enough energy to hop the barrier promoting both vertical and lateral growth (Figure S9b); this criteria is commonly accepted to explain the growth of uncontrolled multi-layers in 2D layered materials at high temperatures. However, this criteria alone cannot explain our results. For instance, the bilayer (and trilayer) lateral heterostructures presented in this work can grow at the same low temperatures as the monolayers (Figure S3), and the number of layers is self-limited for each individual island. Additionally, the TEM analysis at the bilayer heterojunctions (Figures 2k–n, 3h–m, and S8) suggests that the stacked layers have a common lateral growth front.

In order to explain this behavior phenomenologically, we assume that at the early stages of the growth, the initial clusters which serve as nucleation seeds for the islands can have one or few layers. Given the reduced size of these early few-layers clusters, the probability of having adjacent stacked edges, for the bottom and top layers, is high. We expect that adjacent edges will reduce the barrier for adatoms hopping between layers, but the barrier at the uppermost layer is still high enough to prevent adatoms from climbing to the top surface of the structure (Figure 6c,d). The assumption of a lower interlayer barrier for adjacent edges with higher energy barrier at the top edge is reasonable and is equivalent to the shallow periodic potential in crystalline facets with a higher edge-barrier (Schwoebel barrier) in non-van der Waals solids.[56] At low temperatures, this vertical profile of the potential energy allows the diffusion and subsequent attachment of adatoms in all the edges, while the higher energy barrier at the top will prevent the vertical growth of additional layers, resulting in the simultaneous lateral growth of all the layers, with self-limited thickness. Notice that in this scenario, the thickness of the structure is determined by the thickness of the initial cluster. We observed that an increase of the adatoms flux will increase the concentration of bilayers (or multi-layers) lateral heterostructures for the same growth temperature (Figure S4), suggesting that more early nucleation clusters composed of bilayers and multi-layers with respect to monolayers are being randomly formed at the early stages of the growth (Figure S10).

CONCLUSIONS

Looking forward to nanoscale domain sizes synthesized *via* the water-assisted CVD technique used in this work, we have been able to produce superlattices of ultrathin domains (between 200 and 300 nm in lateral size).[57] Smaller domain sizes are possible; however, due to the formation of smooth junctions at the $MoX_2 \rightarrow WX_2$ transitions, a compositional gradient is

DOI: 10.1021/acsnano.9b04957
ACS Nano XXXX, XXX, XXX–XXX

expected for domains with tens of nanometers in width. Further reduction in domain size will require introducing additional modifications such as reverse flow during the transitions between domains in order to avoid the formation of smooth junctions as well as the automation of the gas switching process.

The ability to produce bilayer lateral heterostructures of TMDs, through a relatively simple CVD technique, offers an additional degree of freedom to create complex 2D device architectures and geometries. We have shown that bilayer lateral heterostructures have a superior optoelectronic response when compared to their as-grown monolayer counterparts, for instance, displaying clear photovoltaic and room-temperature electroluminescent responses. Although, the competition between the direct and the indirect electronic transitions in bilayer TMDs is detrimental to their PL quantum efficiency, the addition of an extra layer in 2D lateral heterostructures seems to minimize the role of substrates and adsorbates that could act as additional scattering centers for the charge carriers. It is also quite possible that the bilayers are characterized by smaller Schottky barriers at the level of the electrical contacts. Perhaps, impinging photons interact with both the substrate and the bottom layer reflecting back toward the top layer and from this one to the bottom layer creating some sort of Fabry–Perot resonator.[50] At the moment, we do not have any evidence for this. In any case, a combination of these factors lead to a significant enhancement in the short circuit or photovoltaic currents observed in the bilayers relative to the monolayers. Our observations suggest a promising route to produce more robust and reliable optoelectronic components based on few-layers TMDs that are less sensitive to environmental factors.

METHODS

Synthesis of Bilayer Lateral Heterostructures. All in-plane bilayer lateral heterostructures were synthesized using the one-pot CVD approach recently developed by our group that is described in detail in the ref 9 of the main text. In brief, this method uses water-assisted thermal evaporation of solid sources at atmospheric pressure. Bulk powders of $MoSe_2$ (99.9%, Sigma-Aldrich) and WSe_2 (99.9%, Sigma-Aldrich) were placed together within a high-purity alumina boat and used as solid source precursors to synthesize the bilayer $MoSe_2$-WSe_2 heterostructures, while MoS_2 (99.9%, Sigma-Aldrich) and WS_2 (99.9%, Sigma-Aldrich) were the solid sources for bilayer MoS_2-WS_2 heterostructures. In each case, the powder sources containing 120 mg of MoX_2 and 60 mg of WX_2 (X = S, Se) in a ratio of 2:1, were placed side-by-side within an alumina boat ($L \times W \times H$: 70 × 14 × 10 mm) in the center of a 1 in. diameter horizontal quartz tube furnace. SiO_2/Si (300 nm oxide thickness) substrates were precleaned with acetone, isopropanol, and deionized water. During the growth, the substrates were placed downstream at temperatures ranging between 810 and 780 °C and 6–7 cm away from the solid sources which were maintained at 1060 °C. Initially, the temperature of the furnace was slowly raised up to 1060 °C within 50 min with a constant flow of N_2 (200 sccm), and both, substrates and sources, were kept outside the furnace. When the temperature of the furnace reached above 1040 °C, the solid precursor as well as the substrates were placed at their respective positions, by sliding the quartz tube into the furnace. Simultaneously, water vapor was introduced in a controlled manner by diverting N_2 flow through a bubbler (Sigma-Aldrich) containing 2 mL of DI water at room temperature. In order to switch the growth from Mo- to W-rich compounds, the N_2 + H_2O vapor flux was suddenly replaced by a mixture of Ar + 5% H_2 (200 sccm). Multiple TMD domains were grown by sequentially switching the carrier gases: N_2 + H_2O vapor favors the growth of MoX_2 domains, whereas changing the carrier gas from N_2 + H_2O to Ar + H_2 (5%) favors the growth of WX_2 (X = S or Se). Similar growth conditions were employed for the growth of the selenium-based heterostructures. Once the desired heterostructure sequence was completed, the synthesis process was abruptly terminated by sliding the quartz tube containing both the precursors and the substrates to a cooler zone, while keeping a constant 200 sccm flow of Ar + H_2 (5%) until it cooled down to room temperature.

Raman and Photoluminescence Characterization. The Raman and PL experiments were performed in a confocal microscope-based Raman spectrometer (LabRAM HR Evolution, Horiba Scientific) using a backscattering geometry. An excitation wavelength of 532 nm (laser power at the sample 77 μW) was used and focused with a 100× objective (NA = 0.9, WD = 0.21 mm). During the PL and the Raman mapping, the optical path is stationary, while moving the sample on a computer-controlled motorized *XY* stage.

Transmission Electron Microscopy. High-angle annular scanning transmission electron microscopy (HAADF-STEM) imaging was performed with an aberration-corrected JEOL JEM-ARM200cF with a cold-field emission gun at 200 kV. The STEM resolution of the microscope is 0.78 Å. The HAADF-STEM images were collected with the JEOL HAADF detector using the following experimental conditions: probe size 7 c, condenser lens aperture 30 μm, scan speed 32 μs/pixel, and camera length 8 cm, which corresponds to a probe convergence angle of 21 mrad and inner collection angle of 46 mrad.

Device Fabrication. The electrical contacts to individual MoX_2 and WX_2 domains were fabricated by depositing 80 nm of Au onto a 8 nm thick layer of Ti *via* e-beam evaporation. Contacts were patterned using standard e-beam lithography techniques. After gold deposition, and in order to extract adsorbates, the samples were annealed under high vacuum for 24 h at 120 °C. In order to access the inner domains in the heterostructures without short circuiting with the external ones, as in the case of WSe_2- $MoSe_2$ heterojunctions, thin h-BN crystals were mechanically exfoliated from larger crystals and conveniently placed on the heterostructure before depositing the contacts. The h-BN crystals were grown following the technique developed by Zhigadlo.[49] The technique used to transfer the h-BN onto the heterostructure is similar to the one described by Lee *et al.*[58]

Electrical Characterization. Characterization was performed using a sourcemeter (Keithley 2612 A). For photocurrent measurements, a Coherent Sapphire 532-150 CW CDRH and Thorlabs DLS146-101S were used, with a continuous wavelength λ = 532 nm. Light was transmitted to the sample through a 10 μm single-mode optical fiber with a mode field diameter of 10 μm. The size of the laser spot was also measured against a fine grid.

ASSOCIATED CONTENT

Supporting Information

The Supporting Information is available free of charge on the ACS Publications website at DOI: 10.1021/acsnano.9b04957.

Figures showing the aging effects on monolayers and bilayers, optical absorption on selenides, PL spectra for different number of layers in selenides, thickness statistics as a function of the amount of source materials and distance to the source, additional Raman and PL maps, atomic resolution STEM images of interfaces, electrical characterization of individual domains, SEM and AFM characterization of early stage clusters (PDF)

AUTHOR INFORMATION

Corresponding Authors

*E-mail: humberto3@usf.edu.
*E-mail: balicas@magnet.fsu.edu.
*E-mail: prasanasahoo@gmail.com.

ORCID

Prasana Kumar Sahoo: 0000-0001-6316-7842

DOI: 10.1021/acsnano.9b04957
ACS Nano XXXX, XXX, XXX–XXX

Dmitry Smirnov: 0000-0001-6358-3221
Luis Balicas: 0000-0002-5209-0293
Humberto Rodríguez Gutiérrez: 0000-0001-8997-5274

Present Address

[#]Material Science Centre, Indian Institute of Technology Kharagpur, West Bengal 721302, India

Author Contributions

[▽]These authors contributed equally to this work. P.K.S., L.B., and H.R.G. conceived the idea, designed the experiments, and wrote the manuscript. P.K.S. performed CVD synthesis, Raman, and PL characterizations and related analysis as well as sample preparation for TEM. F.A.N. and T.D.M. performed additional CVD growth, optical characterization, and film transfer. Y.X. and H.R.G. conducted TEM experiments and related data analysis. S.M. and L.B. performed the device design and fabrication, electrical measurements, and related analysis. W. Z. assisted with the device fabrication and testing. Z.L. and D.S. contributed to the EL measurements. N.D.Z. grew the h-BN material used in the devices. All authors discussed the results and commented on the manuscript.

Notes

The authors declare no competing financial interest.

ACKNOWLEDGMENTS

H.R.G. acknowledges support by the National Science Foundation grant DMR-1557434 (CAREER: Two-Dimensional Heterostructures Based on Transition-Metal Dichalcogenides). L.B. acknowledges support from Army Research Office through MURI award W911NF-11-1-0362 (Synthesis of 2D materials), the Office of Naval Research through DURIP grant no. 11997003 (transfer and stacking under inert conditions), and the National Science Foundation through DMR- 1807969 (synthesis and graduate student support). TEM work was performed at the NHMFL which is supported by the NSF Cooperative Agreement no. DMR-1644779 and the State of Florida.

REFERENCES

(1) Kang, K.; Xie, S.; Huang, L.; Han, Y.; Huang, P. Y.; Mak, K. F.; Kim, C. J.; Muller, D.; Park, J. High-Mobility Three-Atom-Thick Semiconducting Films with Wafer-Scale Homogeneity. *Nature* **2015**, *520*, 656−660.

(2) Schmidt, H.; Wang, S.; Chu, L.; Toh, M.; Kumar, R.; Zhao, W.; Castro Neto, A. H.; Martin, J.; Adam, S.; Ozyilmaz, B.; Eda, G. Transport Properties of Monolayer MoS_2 Grown by Chemical Vapor Deposition. *Nano Lett.* **2014**, *14*, 1909−1913.

(3) Duan, X. D.; Wang, C.; Shaw, J. C.; Cheng, R.; Chen, Y.; Li, H. L.; Wu, X. P.; Tang, Y.; Zhang, Q. L.; Pan, A. L.; Jiang, J. H.; Yu, R. Q.; Huang, Y.; Duan, X. F. Lateral Epitaxial Growth of Two-Dimensional Layered Semiconductor Heterojunctions. *Nat. Nanotechnol.* **2014**, *9*, 1024−1030.

(4) Gong, Y. J.; Lin, J. H.; Wang, X. L.; Shi, G.; Lei, S. D.; Lin, Z.; Zou, X. L.; Ye, G. L.; Vajtai, R.; Yakobson, B. I.; Terrones, H.; Terrones, M.; Tay, B. K.; Lou, J.; Pantelides, S. T.; Liu, Z.; Zhou, W.; Ajayan, P. M. Vertical and In-Plane Heterostructures from WS_2/MoS_2 Monolayers. *Nat. Mater.* **2014**, *13*, 1135−1142.

(5) Gong, Y. J.; Lei, S. D.; Ye, G. L.; Li, B.; He, Y. M.; Keyshar, K.; Zhang, X.; Wang, Q. Z.; Lou, J.; Liu, Z.; Vajtai, R.; Zhou, W.; Ajayan, P. M. Two-Step Growth of Two-Dimensional $WSe_2/MoSe_2$ Heterostructures. *Nano Lett.* **2015**, *15*, 6135−6141.

(6) Huang, C. M.; Wu, S. F.; Sanchez, A. M.; Peters, J. J. P.; Beanland, R.; Ross, J. S.; Rivera, P.; Yao, W.; Cobden, D. H.; Xu, X. D. Lateral Heterojunctions within Monolayer $MoSe_2$-WSe_2 Semiconductors. *Nat. Mater.* **2014**, *13*, 1096−1101.

(7) Li, M. Y.; Shi, Y. M.; Cheng, C. C.; Lu, L. S.; Lin, Y. C.; Tang, H. L.; Tsai, M. L.; Chu, C. W.; Wei, K. H.; He, J. H.; Chang, W. H.; Suenaga, K.; Li, L. J. Epitaxial Growth of a Monolayer WSe_2-MoS_2 Lateral p−n Junction with an Atomically Sharp Interface. *Science* **2015**, *349*, 524−528.

(8) Zhang, Z.; Chen, P.; Duan, X.; Zang, K.; Luo, J.; Duan, X. Robust Epitaxial Growth of Two-Dimensional Heterostructures, Multiheterostructures, and Superlattices. *Science* **2017**, *357*, 788−792.

(9) Sahoo, P. K.; Memaran, S.; Xin, Y.; Balicas, L.; Gutierrez, H. R. One-Pot Growth of Two-Dimensional Lateral Heterostructures *via* Sequential Edge-Epitaxy. *Nature* **2018**, *553*, 63−67.

(10) Xie, S.; Tu, L.; Han, Y.; Huang, L.; Kang, K.; Lao, K. U.; Poddar, P.; Park, C.; Muller, D. A.; DiStasio, R. A., Jr.; Park, J. Coherent, Atomically Thin Transition-Metal Dichalcogenide Superlattices with Engineered Strain. *Science* **2018**, *359*, 1131−1136.

(11) Brar, V. W.; Sherrott, M. C.; Jariwala, D. Emerging Photonic Architectures in Two-Dimensional Opto-Electronics. *Chem. Soc. Rev.* **2018**, *47*, 6824−6844.

(12) Zhou, Y.; Tan, H.; Sheng, Y.; Fan, Y.; Xu, W.; Warner, J. H. Utilizing Interlayer Excitons in Bilayer WS_2 for Increased Photovoltaic Response in Ultrathin Graphene Vertical Cross-Bar Photodetecting Tunneling Transistors. *ACS Nano* **2018**, *12*, 4669−4677.

(13) Wong, J.; Jariwala, D.; Tagliabue, G.; Tat, K.; Davoyan, A. R.; Sherrott, M. C.; Atwater, H. A. High Photovoltaic Quantum Efficiency in Ultrathin Van Der Waals Heterostructures. *ACS Nano* **2017**, *11*, 7230−7240.

(14) Gao, Q.; Zhang, Z.; Xu, X.; Song, J.; Li, X.; Wu, Y. Scalable High Performance Radio Frequency Electronics Based on Large Domain Bilayer MoS_2. *Nat. Commun.* **2018**, *9*, 4778.

(15) Kim, S.; Konar, A.; Hwang, W. S.; Lee, J. H.; Lee, J.; Yang, J.; Jung, C.; Kim, H.; Yoo, J. B.; Choi, J. Y.; Jin, Y. W.; Lee, S. Y.; Jena, D.; Choi, W.; Kim, K. High-Mobility and Low-Power Thin-Film Transistors Based on Multilayer MoS_2 Crystals. *Nat. Commun.* **2012**, *3*, 1011.

(16) Zhang, X.; Nan, H.; Xiao, S.; Wan, X.; Gu, X.; Du, A.; Ni, Z.; Ostrikov, K. K. Transition Metal Dichalcogenides Bilayer Single Crystals by Reverse-Flow Chemical Vapor Epitaxy. *Nat. Commun.* **2019**, *10*, 598.

(17) Zhu, B. R.; Zeng, H. L.; Dai, J. F.; Gong, Z. R.; Cui, X. D. Anomalously Robust Valley Polarization and Valley Coherence in Bilayer WS_2. *Proc. Natl. Acad. Sci. U. S. A.* **2014**, *111*, 11606−11611.

(18) Wu, S. F.; Ross, J. S.; Liu, G. B.; Aivazian, G.; Jones, A.; Fei, Z. Y.; Zhu, W. G.; Xiao, D.; Yao, W.; Cobden, D.; Xu, X. D. Electrical Tuning of Valley Magnetic Moment Through Symmetry Control in Bilayer MoS_2. *Nat. Phys.* **2013**, *9*, 149−153.

(19) Alexeev, E. M.; Ruiz-Tijerina, D. A.; Danovich, M.; Hamer, M. J.; Terry, D. J.; Nayak, P. K.; Ahn, S.; Pak, S.; Lee, J.; Sohn, J. I.; Molas, M. R.; Koperski, M.; Watanabe, K.; Taniguchi, T.; Novoselov, K. S.; Gorbachev, R. V.; Shin, H. S.; Fal'ko, V. I.; Tartakovskii, A. I. Resonantly Hybridized Excitons in Moire Superlattices in Van Der Waals Heterostructures. *Nature* **2019**, *567*, 81−86.

(20) Jin, C.; Regan, E. C.; Yan, A.; Iqbal Bakti Utama, M.; Wang, D.; Zhao, S.; Qin, Y.; Yang, S.; Zheng, Z.; Shi, S.; Watanabe, K.; Taniguchi, T.; Tongay, S.; Zettl, A.; Wang, F. Observation of Moire Excitons in WSe_2/WS_2 Heterostructure Superlattices. *Nature* **2019**, *567*, 76−80.

(21) Seyler, K. L.; Rivera, P.; Yu, H.; Wilson, N. P.; Ray, E. L.; Mandrus, D. G.; Yan, J.; Yao, W.; Xu, X. Signatures of Moire-Trapped Valley Excitons in $MoSe_2/WSe_2$ Heterobilayers. *Nature* **2019**, *567*, 66−70.

(22) Tran, K.; Moody, G.; Wu, F.; Lu, X.; Choi, J.; Kim, K.; Rai, A.; Sanchez, D. A.; Quan, J.; Singh, A.; Embley, J.; Zepeda, A.; Campbell, M.; Autry, T.; Taniguchi, T.; Watanabe, K.; Lu, N.; Banerjee, S. K.; Silverman, K. L.; Kim, S.; Tutuc, E.; Yang, L.; MacDonald, A. H.; Li, X. Evidence for Moire Excitons in Van Der Waals Heterostructures. *Nature* **2019**, *567*, 71−75.

(23) Wu, F. C.; Lovorn, T.; MacDonald, A. H. Topological Exciton Bands in Moire Heterojunctions. *Phys. Rev. Lett.* **2017**, *118*, 147401.

DOI: 10.1021/acsnano.9b04957
ACS Nano XXXX, XXX, XXX−XXX

(24) Unuchek, D.; Ciarrocchi, A.; Avsar, A.; Watanabe, K.; Taniguchi, T.; Kis, A. Room-Temperature Electrical Control of Exciton Flux in a Van Der Waals Heterostructure. *Nature* **2018**, *560*, 340−344.
(25) Kufer, D.; Konstantatos, G. Highly Sensitive, Encapsulated MoS_2 Photodetector with Gate Controllable Gain and Speed. *Nano Lett.* **2015**, *15*, 7307−7313.
(26) Radisavljevic, B.; Radenovic, A.; Brivio, J.; Giacometti, V.; Kis, A. Single-Layer MoS_2 Transistors. *Nat. Nanotechnol.* **2011**, *6*, 147−150.
(27) Perea-Lopez, N.; Elias, A. L.; Berkdemir, A.; Castro-Beltran, A.; Gutierrez, H. R.; Feng, S. M.; Lv, R. T.; Hayashi, T.; Lopez-Urias, F.; Ghosh, S.; Muchharla, B.; Talapatra, S.; Terrones, H.; Terrones, M. Photosensor Device Based on Few-Layered WS_2 Films. *Adv. Funct. Mater.* **2013**, *23*, 5511−5517.
(28) Liu, E. F.; Long, M. S.; Zeng, J. W.; Luo, W.; Wang, Y. J.; Pan, Y. M.; Zhou, W.; Wang, B. G.; Hu, W. D.; Ni, Z. H.; You, Y. M.; Zhang, X. A.; Qin, S. Q.; Shi, Y.; Watanabe, K.; Taniguchi, T.; Yuan, H. T.; Hwang, H. Y.; Cui, Y.; Miao, F.; Xing, D. Y. High Responsivity Phototransistors Based on Few-Layer ReS2 for Weak Signal Detection. *Adv. Funct. Mater.* **2016**, *26*, 1938−1944.
(29) Pradhan, N. R.; Ludwig, J.; Lu, Z. G.; Rhodes, D.; Bishop, M. M.; Thirunavukkuarasu, K.; McGill, S. A.; Smirnov, D.; Balicas, L. High Photoresponsivity and Short Photoresponse Times in Few-Layered WSe_2 Transistors. *ACS Appl. Mater. Interfaces* **2015**, *7*, 12080−12088.
(30) Xu, K.; Wang, Z. X.; Wang, F.; Huang, Y.; Wang, F. M.; Yin, L.; Jiang, C.; He, J. Ultrasensitive Phototransistors Based on Few-Layered HfS_2. *Adv. Mater.* **2015**, *27*, 7881−7887.
(31) Castellanos-Gomez, A.; Quereda, J.; van der Meulen, H. P.; Agrait, N.; Rubio-Bollinger, G. Spatially Resolved Optical Absorption Spectroscopy of Single- and Few-Layer MoS_2 by Hyperspectral Imaging. *Nanotechnology* **2016**, *27*, 115705.
(32) Berkdemir, A.; Gutierrez, H. R.; Botello-Mendez, A. R.; Perea-Lopez, N.; Elias, A. L.; Chia, C. I.; Wang, B.; Crespi, V. H.; Lopez-Urias, F.; Charlier, J. C.; Terrones, H.; Terrones, M. Identification of Individual and Few Layers of WS_2 Using Raman Spectroscopy. *Sci. Rep.* **2013**, *3*, 1755.
(33) Zhao, W.; Ghorannevis, Z.; Amara, K. K.; Pang, J. R.; Toh, M.; Zhang, X.; Kloc, C.; Tan, P. H.; Eda, G. Lattice Dynamics in Mono- and Few-Layer Sheets of WS_2 and WSe_2. *Nanoscale* **2013**, *5*, 9677−9683.
(34) Lee, C.; Yan, H.; Brus, L. E.; Heinz, T. F.; Hone, J.; Ryu, S. Anomalous Lattice Vibrations of Single- and Few-Layer MoS_2. *ACS Nano* **2010**, *4*, 2695−2700.
(35) Carvalho, B. R.; Wang, Y.; Mignuzzi, S.; Roy, D.; Terrones, M.; Fantini, C.; Crespi, V. H.; Malard, L. M.; Pimenta, M. A. Intervalley Scattering by Acoustic Phonons in Two-Dimensional MoS_2 Revealed by Double-Resonance Raman Spectroscopy. *Nat. Commun.* **2017**, *8*, 14670.
(36) Chakraborty, B.; Bera, A.; Muthu, D. V. S.; Bhowmick, S.; Waghmare, U. V.; Sood, A. K. Symmetry-Dependent Phonon Renormalization in Monolayer MoS_2 Transistor. *Phys. Rev. B: Condens. Matter Mater. Phys.* **2012**, *85*, No. 161403(R).
(37) Mignuzzi, S.; Pollard, A. J.; Bonini, N.; Brennan, B.; Gilmore, I. S.; Pimenta, M. A.; Richards, D.; Roy, D. Effect of Disorder on Raman Scattering of Single-Layer MoS_2. *Phys. Rev. B: Condens. Matter Mater. Phys.* **2015**, *91*, 195411.
(38) Zhao, W.; Ribeiro, R. M.; Toh, M.; Carvalho, A.; Kloc, C.; Castro Neto, A. H.; Eda, G. Origin of Indirect Optical Transitions in Few-Layer MoS_2, WS_2, and WSe_2. *Nano Lett.* **2013**, *13*, 5627−5634.
(39) Gutierrez, H. R.; Perea-Lopez, N.; Elias, A. L.; Berkdemir, A.; Wang, B.; Lv, R.; Lopez-Urias, F.; Crespi, V. H.; Terrones, H.; Terrones, M. Extraordinary Room-Temperature Photoluminescence in Triangular WS_2 Monolayers. *Nano Lett.* **2013**, *13*, 3447−3454.
(40) Mak, K. F.; Lee, C.; Hone, J.; Shan, J.; Heinz, T. F. Atomically Thin MoS_2: A New Direct-Gap Semiconductor. *Phys. Rev. Lett.* **2010**, *105*, 136805.
(41) Kim, M. S.; Yun, S. J.; Lee, Y.; Seo, C.; Han, G. H.; Kim, K. K.; Lee, Y. H.; Kim, J. Biexciton Emission from Edges and Grain Boundaries of Triangular WS_2 Monolayers. *ACS Nano* **2016**, *10*, 2399−2405.
(42) Katzke, H.; Toledano, P.; Depmeier, W. Phase Transitions Between Polytypes and Intralayer Superstructures in Transition Metal Dichalcogenides. *Phys. Rev. B: Condens. Matter Mater. Phys.* **2004**, *69*, 134111.
(43) Howell, S. L.; Jariwala, D.; Wu, C. C.; Chen, K. S.; Sangwan, V. K.; Kang, J.; Marks, T. J.; Hersam, M. C.; Lauhon, L. J. Investigation of Band-Offsets at Monolayer-Multilayer MoS_2 Junctions by Scanning Photocurrent Microscopy. *Nano Lett.* **2015**, *15*, 2278−2284.
(44) Sahin, H.; Tongay, S.; Horzum, S.; Fan, W.; Zhou, J.; Li, J.; Wu, J.; Peeters, F. M. Anomalous Raman Spectra and Thickness-Dependent Electronic Properties of WSe_2. *Phys. Rev. B: Condens. Matter Mater. Phys.* **2013**, *87*, 165409.
(45) Tonndorf, P.; Schmidt, R.; Bottger, P.; Zhang, X.; Borner, J.; Liebig, A.; Albrecht, M.; Kloc, C.; Gordan, O.; Zahn, D. R. T.; Michaelis de Vasconcellos, S.; Bratschitsch, R. Photoluminescence Emission and Raman Response of Monolayer MoS_2, $MoSe_2$, and WSe_2. *Opt. Express* **2013**, *21*, 4908−4916.
(46) Zeng, Z. X. S.; Sun, X. X.; Zhang, D. L.; Zheng, W. H.; Fan, X. P.; He, M.; Xu, T.; Sun, L. T.; Wang, X.; Pan, A. L. Controlled Vapor Growth and Nonlinear Optical Applications of Large-Area 3R Phase WS_2 and WSe_2 Atomic Layers. *Adv. Funct. Mater.* **2019**, *29*, 1806874.
(47) Govind Rajan, A.; Warner, J. H.; Blankschtein, D.; Strano, M. S. Generalized Mechanistic Model for the Chemical Vapor Deposition of 2D Transition Metal Dichalcogenide Monolayers. *ACS Nano* **2016**, *10*, 4330−4344.
(48) Wang, S.; Rong, Y.; Fan, Y.; Pacios, M.; Bhaskaran, H.; He, K.; Warner, J. H. Shape Evolution of Monolayer MoS_2 Crystals Grown by Chemical Vapor Deposition. *Chem. Mater.* **2014**, *26*, 6371−6379.
(49) Zhigadlo, N. D. Crystal Growth of Hexagonal Boron Nitride (hBN) from Mg-B-N Solvent System Under High Pressure. *J. Cryst. Growth* **2014**, *402*, 308−311.
(50) Jariwala, D.; Davoyan, A. R.; Wong, J.; Atwater, H. A. Van Der Waals Materials for Atomically-Thin Photovoltaics: Promise and Outlook. *ACS Photonics* **2017**, *4*, 2962−2970.
(51) Memaran, S.; Pradhan, N. R.; Lu, Z. G.; Rhodes, D.; Ludwig, J.; Zhou, Q.; Ogunsolu, O.; Ajayan, P. M.; Smirnov, D.; Fernandez-Dominguez, A. I.; Garcia-Vidal, F. J.; Balicas, L. Pronounced Photovoltaic Response from Multilayered Transition-Metal Dichalcogenides p−n Junctions. *Nano Lett.* **2015**, *15*, 7532−7538.
(52) Wu, C. C.; Jariwala, D.; Sangwan, V. K.; Marks, T. J.; Hersam, M. C.; Lauhon, L. J. Elucidating the Photoresponse of Ultrathin MoS_2 Field-Effect Transistors by Scanning Photocurrent Microscopy. *J. Phys. Chem. Lett.* **2013**, *4*, 2508−2513.
(53) Shang, S. L.; Lindwall, G.; Wang, Y.; Redwing, J. M.; Anderson, T.; Liu, Z. K. Lateral *Versus* Vertical Growth of Two-Dimensional Layered Transition-Metal Dichalcogenides: Thermodynamic Insight into MoS_2. *Nano Lett.* **2016**, *16*, 5742−5750.
(54) Ye, H.; Zhou, J.; Er, D.; Price, C. C.; Yu, Z.; Liu, Y.; Lowengrub, J.; Lou, J.; Liu, Z.; Shenoy, V. B. Toward a Mechanistic Understanding of Vertical Growth of Van Der Waals Stacked 2D Materials: A Multiscale Model and Experiments. *ACS Nano* **2017**, *11*, 12780−12788.
(55) Nie, Y.; Liang, C.; Cha, P. R.; Colombo, L.; Wallace, R. M.; Cho, K. A Kinetic Monte Carlo Simulation Method of Van Der Waals Epitaxy for Atomistic Nucleation-Growth Processes of Transition Metal Dichalcogenides. *Sci. Rep.* **2017**, *7*, 2977.
(56) Schwoebel, R. L.; Shipsey, E. J. Step Motion on Crystal Surfaces. *J. Appl. Phys.* **1966**, *37*, 3682−3686.
(57) Sahoo, P. K.; Zong, H. N.; Liu, J. R.; Xue, W. J.; Lai, X. Y.; Gutierrez, H. R.; Voronine, D. V. Probing Nano-Heterogeneity and Aging Effects in Lateral 2D Heterostructures Using Tip-Enhanced Photoluminescence. *Opt. Mater. Express* **2019**, *9*, 1620−1631.
(58) Lee, C. H.; Lee, G. H.; van der Zande, A. M.; Chen, W. C.; Li, Y. L.; Han, M. Y.; Cui, X.; Arefe, G.; Nuckolls, C.; Heinz, T. F.; Guo,

DOI: 10.1021/acsnano.9b04957
ACS Nano XXXX, XXX, XXX−XXX

J.; Hone, J.; Kim, P. Atomically Thin p−n Junctions with Van Der Waals Heterointerfaces. *Nat. Nanotechnol.* **2014**, *9*, 676−681.

DOI: 10.1021/acsnano.9b04957
ACS Nano XXXX, XXX, XXX−XXX